Charge Transport by Polyatomic Anion Diffusion in $Sc_2(WO_4)_3$

Yongkai Zhou,[†] Stefan Adams,*[,†] R. Prasada Rao,[†] Doreen D. Edwards,[‡] Arkady Neiman,[§] and N. Pestereva[§]

Department of Materials Science and Engineering, National University of Singapore, Singapore 117574, Department of Materials Science and Engineering, Alfred University, Alfred, New York 14802, and Chemical Department, Ural State University, 620083, Ekaterinburg, Russia

Received February 16, 2008. Revised Manuscript Received July 31, 2008

Discussions about the nature of the charge carriers in the scandium tungstate and other isostructural tungstates and molybdates have persisted in the literature since a variety of experimental indications pointed toward trivalent cations as the mobile species. Here variations of the structure over a wide temperature range are analyzed by XRD and computational methods, demonstrating that the negative thermal expansion persists throughout the range of 11−1300 K. Over a limited temperature range (<500 K) molecular dynamics simulations with an optimized forcefield reproduce this negative thermal expansion. Likewise, charge transport is monitored both experimentally by impedance spectroscopy and Tubandt experiments and computationally based on the molecular dynamics simulation trajectories. Extended isothermal−isobaric simulations suggest a complex migration of polyatomic tungstate anions as the energetically most favorable transport mechanism in $Sc_2(WO_4)_3$. A bond valence analysis depicts possible diffusion pathways for WO_4^{2-}, although there is no indication of a pathway for Sc^{3+}. The hopping mechanism of tungstate ions from one equilibrium site to another one follows the instantaneous diffusion pathways. A long-range transport still requires the rare formation of WO_4^{2-} Frenkel defects limiting the accuracy of the simulated absolute conductivity. Both MD simulations and bond valence analysis suggest WO_4^{2-} be the mobile species, which follow the interstitialcy diffusion mechanism. Our 3-section Tubandt-type experiments qualitatively show that the transfer of W occurs in the form of a negatively charged complex. This should be the first example of polyatomic diffusion species and opens a new field in the search for new ionic conductors.

1. Introduction

The ion transport mechanism in $A_2(MO_4)_3$ oxides with the scandium tungstate structure, where A represents trivalent Sc^{3+}, In^{3+}, Al^{3+}, or rare earth cations RE^{3+}, and M is usually W^{6+} or Mo^{6+}, has been the subject of detailed investigations following recent reports that trivalent cations could be the mobile charge carriers in these compounds.[1−9] Because of their high charge, trivalent ions should, however, have strong interactions with surrounding anions and thus they are generally considered to be immobile species in solid ion conductors. Several experimental findings indeed seem to support the claimed mobility of the trivalent cations in the solid state: DC polarization experiments using blocking electrodes confirm that ion transport is predominantly ionic (electronic contribution <8% for A = Sc and ≪1% for A = In).[1−3,10] A cross-sectional electron probe microanalysis[2,4] shows that Sc is enriched at the interface between the solid electrolyte and the cathode. It should however be noted that this phenomenon can be explained by either Sc migrating to the cathode or by the anions moving away from the cathode and thus leaving a higher concentration of Sc behind. The formation energy of Sc Frenkel defects (10.1 eV) or the migration energies of Sc vacancies (7.7 eV) are unrealistically high, whereas Sc interstitials, once formed, could be mobile though still with an activation energy (1.02 eV) that is about twice the experimentally observed value and there is no indication that low-energy defects in $A_2(MO_4)_3$ can be formed by aliovalent doping with A^{2+} cations.[11] Thus there is no physically plausible explanation for the formation of trivalent mobile defects in the scandium tungstate structure.

An alternative explanation of ionic conductivity as originating from O^{2-} mobility is not consistent with the

* Corresponding author. E-mail: mseasn@nus.edu.sg. Tel: (65) 6516 6869. Fax: (65) 6776 3604.
[†] National University of Singapore.
[‡] Alfred University.
[§] Ural State University.

(1) Imanaka, N.; Kobayashi, Y.; Adachi, G. Y. *Chem. Lett.* **1995**, *24*, 433–434.
(2) Imanaka, N.; Kobayashi, Y.; Fujiwara, K.; Asano, T.; Okazaki, Y.; Adachi, G. Y. *Chem. Mater.* **1998**, *10*, 2006–2012.
(3) Köhler, J.; Imanaka, N.; Adachi, G. *Z. Anorg. Allg. Chem.* **1999**, *625*, 1890–1896.
(4) Köhler, J.; Imanaka, N.; Adachi, G. Y. *J. Mater. Chem.* **1999**, *9*, 1357–1362.
(5) Kobayashi, Y.; Egawa, T.; Tamura, S.; Imanaka, N.; Adachi, G. Y. *Chem. Mater.* **1997**, *9*, 1649–1654.
(6) Kobayashi, Y.; Egawa, T.; Okazaki, Y.; Tamura, S.; Imanaka, I.; Adachi, G. *Solid State Ionics* **1998**, *111*, 59–65.
(7) Tamura, S.; Egawa, T.; Okazaki, Y.; Kobayashi, Y.; Imanaka, N.; Adachi, G. *Chem. Mater.* **1998**, *10*, 1958–1962.
(8) Adachi, G.; Köhler, J.; Imanaka, N. *Electrochemistry* **1999**, *67*, 744–751.
(9) Imanaka, N.; Kobayashi, Y.; Tamura, S.; Adachi, G. *Solid State Ionics* **2000**, *136*, 319–324.
(10) Kulikova, T.; Neiman, A.; Kartavtseva, A.; Edwards, D.; Adams, S. *Solid State Ionics* **2008**, *178*, 1714–1718.
(11) Driscoll, D. J.; Islam, M. S.; Slater, P. R. *Solid State Ionics* **2005**, *176*, 539–546.

10.1021/cm800466y CCC: $40.75
Published on Web 09/23/2008

experimental finding that a variation in the oxygen partial pressure over 10−15 orders of magnitude (for the isostructural case of $In_2(WO_4)_3$ see Kulikova et al.[10]) does not affect the conductivity, although it should significantly alter the concentration of oxygen vacancies. Moreover, Driscoll et al.[11] predict a high activation energy for the formation of O^{2-} Frenkel defects.

The attribution of either Sc^{3+} or O^{2-} as being the mobile species rests on the postulate that only monatomic species can be responsible for the charge transport. As both of these hypotheses seem to lead to controversial experimental findings, the interpretations of the experimental and computational results have to be fundamentally revisited. Although size, mass, and charge density are all critical factors affecting the mobility of charge carriers, the mobility of alternative polyatomic charge carriers cannot be ruled out. This has been indicated previously for Scheelite ($CaWO_4$) and related tungstates in the work by Neiman.[12] WO_3 is volatile when heated to high temperature and thus many tungstates have a tendency to lose WO_3 at elevated temperatures, which will lead to the formation of WO_x "quasi-molecules" with $x < 4$ in the solid state that might exhibit some mobility in various Scheelite-related tungstates. Neiman proposed that such "quasi-molecules" and thereby essentially W might move via the rearrangement of tungsten oxygen bonds causing inversions and rearrangements of the WO_x group.[12]

A further indication of the local mobilities of the different species can be read from the fact that phases for which the mobility of highly charged cations has been claimed in the literature generally exhibit the otherwise unusual negative thermal expansion (NTE).[13−15] This NTE behavior was also found in all $Sc_2(WO_4)_3$ type structure materials over certain temperature range. Evans[13] explains the NTE in this structure type as a consequence of large amplitude thermal vibrations of the oxygen atoms perpendicular to the W−O−Sc axis linking WO_4 tetrahedra with ScO_6 octahedra. As the W−O bond is more covalent than the Sc−O, it is to be expected that WO_4 will be a more rigid group than ScO_6 in the $Sc_2(WO_4)_3$ structure. Therefore, it may be speculated that the entire WO_4^{2-} unit does not only exhibit large amplitude rocking motion in this open framework structure, but could also be regarded as a potentially mobile species.

In this work, we will use a combination of diffraction and electrochemical experiments with atomistic simulations to test the various conceivable ion transport mechanisms. In situ powder diffraction studies provide the information on the variation of the crystal structure with temperature, and impedance spectroscopy as well as DC electrolysis experiments are employed to study the conductivity. Computational studies then aim at reproducing the experimentally observed structural features (e.g., negative thermal expansion behavior) and reveal the atomic scale conduction mechanism. Here, we combine empirical molecular dynamics simulations with a fine-tuned force-field with bond valence transport pathway analyses. Previous studies demonstrated that bond valence analyses are a useful tool to identify the mobile species as they provide a visualization of the diffusion pathways. In simple cases, they may be applied to static structure models,[16−20] whereas detailed studies of more complex transport mechanisms involving reorganizations of both cations and anions require a dynamic pathway analysis. Preliminary results of such a bond valence pathway analysis for $Sc_2(WO_4)_3$ based on the static average crystal structure have been reported by us recently.[16] Here, dynamic transport pathways for both Sc^{3+} and WO_4^{2-} will be analyzed in detail based on molecular dynamics trajectories, whereas pathway models for other less likely mobile species such as O^{2-} or W^{6+} are discussed only briefly based on static structure snapshots.

2. Methods

2.1. Experimental. $Sc_2(WO_4)_3$ sample pellets are prepared by conventional solid-state techniques, from the mixture of stoichiometric amounts of Sc_2O_3 (purity 99.99%, Grirem) and WO_3 (purity 99.9%, Fluka) by repeated grinding and firing at 1000 °C. Using the inverted crucible technique the atmosphere around the sample was saturated with WO_3 to prevent an evaporation of WO_3 from the sample. The sample pellets were then characterized by in situ X-ray powder diffractometry using Cu Kα radiation (PANalytical X'Pert PRO) equipped with a fast linear detector (X'Celerator), which can collect 100 steps simultaneously. XRD data were collected in the 2θ range 10−120° with a nominal scan rate of 70 s/step and a step size of 0.017° for temperatures in the range from 11 to 1300 K in 50 K intervals. Data for temperatures up to 300 K are measured in an Oxford cryosystems cooling stage, while data for the high temperature range are measured in a heating chamber (Anton Paar HTK 1200N). Both heating and cooling chambers had to be evacuated during the measurement. The temperature variation at the sample position inside the oven chamber is within 2−3% of the heating element temperature.[21] Rietveld refinements of XRD powder patterns are performed with the Generalized Structure Analysis System (GSAS) by Larson and von Dreele,[22] along with the graphical user interface EXPGUI.[23] Structure data from published neutron diffraction measurements by Evans et al.[13] for the temperature range 10 − 450K were used as the starting point of the refinement. Measurement conditions and refinement procedures are standardized to avoid that differences affect the observed dependence of structure details on temperature. All structures at different temperatures are thus refined based on the same

(12) Neiman, A. Y. *Solid State Ionics* **1996**, *83*, 263–273.
(13) Evans, J. S. O.; Mary, T. A.; Sleight, A. W. *J. Solid State Chem.* **1998**, *137*, 148–160.
(14) Evans, J. S. O. *J. Chem. Soc., Dalton Trans.* **1999**, 3317–3326.
(15) Evans, J. S. O.; Mary, T. A.; Sleight, A. W. *J. Solid State Chem.* **1997**, *133*, 580–583.
(16) Adams, S. *Solid State Ionics* **2006**, *177*, 1625–1630.
(17) Adams, S.; Swenson, J. *Phys. Rev. Lett.* **2000**, *84*, 4144–4147.
(18) Thangadurai, V.; Adams, S.; Weppner, W. *Chem. Mater.* **2004**, *16*, 2998–3006.
(19) Hall, A.; Adams, S.; Swenson, J. *Phys. Rev. B* **2006**, 74.
(20) Adams, S.; Swenson, J. *Solid State Ionics* **2002**, *154*, 151–159.
(21) Fantner, E. B.; Koppelhuber-Bitschnau, B.; Mautner, F. A.; Doppler, P.; Gautsch, J. *Mater. Sci. Forum* **1998**, *278*−*2*, 260–263.
(22) Larson, A. C.; von Dreele, R. B. *General Structure Analysis System (GSAS)*; Report LAUR 86-748; Los Alamos National Laboratory: Los Alamos, NM, 2000.
(23) Toby, B. *J. Appl. Crystallogr.* **2001**, *34*, 210–213.

set of 52 refinable parameters: 12 background variables of a shifted Chebyschev function, 7 profile variables, 3 cell parameters, 25 refinable atomic coordinates, 3 atomic displacement parameters, 1 preferential orientation parameter, and an overall scale factor. Impedance spectra are recorded with a Solartron SI 1260 impedance analyzer, using sintered pellets with sputtered platinum electrodes as ion blocking electrode on both sides. Measurements were carried out over frequency range from 1 Hz to 1 MHz in the temperature range from 550 to 1300 K in steps of 25 K.

For each Tubandt measurement, three disks of $Sc_2(WO_4)_3$ ceramics with polished surfaces were inserted between Pt electrodes. The typical thickness of an individual disk was 1.4 mm. A voltage of 300 V was applied for 21−48 h at a temperature in the range 940−990 °C. Currents were limited to 1 mA but in most cases average currents were only about 0.1 mA because of the low conductivity of $Sc_2(WO_4)_3$ disks. The relative porosity of the samples did not exceed 0.2. The Gorelov's modified EMF technique[24] (which uses an external active load to minimizes the effect of electrode polarization) was used to redetermine the ionic transference number.

2.2. Computer Simulation. Molecular dynamics simulations for a 1224 atom ($3a \times 2b \times 3c$) supercell were performed using the Cerius[2] (for isothermal−isobaric, NPT) and Materials Studio (for isothermal-isochoric, NVT) software suites by Accelrys,[25,26] using the same parameters based on a modified UFF universal forcefield as discussed in section 3.2.1.[27] Integration of the equation of motion has been performed with a Verlet velocity algorithm[28] in Materials Studio or a Verlet leapfrog algorithm in Cerius[2]. Time steps have been chosen as 1.5 fs for the evaluation of the diffusion coefficients or 1.0 fs for the transport mechanism investigation. Coulombic interactions have been calculated by the Ewald summation method with a cutoff of 12.5 Å and an accuracy of 0.001 kcal/mol and a short-range interaction cutoff of 5.61 Å. Temperature is controlled using the Nosé−Hoover thermostat and pressure (for the case of the NPT simulations) by the Parrinello−Rahman barostat (Cell mass prefactor = 10). For the assessment of diffusion coefficients NVT simulations are run for 8.5 ns (for T = 1350 K) to 13.5 ns (for T = 1200 K).

Diffusion pathways were studied by bond valence analysis. The bond valence for each bond between neighboring cation and anion can be calculated from

$$s_{A-X} = \exp\left[\frac{R_0 - R}{b}\right] \quad (1)$$

where R is the distance between counterions A and X.[29] R_0 (the bond length for which s_{A-X} is one), and b (which in our softBV parameter set characterizes the bond softness) are tabulated empirical softBV parameters refined from sets of reference structures.[30,31] Specially refined parameter values for the $Sc^{3+}-WO_4^{2-}$ interaction (R_0 = 3.39949 Å, b = 0.5 Å, cutoff radius 7 Å)[16] are used to test the mobility of WO_4^{2-} ions, treating it as a pseudoatom. The bond valence sum (BVS) of the ion A is then defined by

$$V = \sum_X s_{A-X} \quad (2)$$

where the summation runs over all counterions X within a cutoff distance from the central atom A. In contrast to other bond valence tables, the cutoff radii chosen in the softBV parameter set include higher coordination shells, which helps to avoid unphysical stepwise changes of the BVS calculated for a moving particle when it crosses the boundary of its original first coordination shell. The BVS mismatch threshold that a mobile ion has to cross between equilibrium sites is associated with the activation energy for the migration process. An additional penalty function p_{A-X} has to be included to penalize highly asymmetric coordinations where a matching BVS is reached but one of the bonds becomes unrealistically short.

$$|\Delta V(A)| = |\sum_X s_{A-X} - V_{id}(A)| + \sum_X p_{A-X} \quad (3)$$

$$p_{A-X} = \begin{cases} \left(s_{A-X} - \dfrac{V_{id}}{CN_{min}}\right)^2 & \text{, if } s_{A-X} > \dfrac{V_{id}}{CN_{min}} \\ 0 & \text{, if } s_{A-X} < \dfrac{V_{id}}{CN_{min}} \end{cases} \quad (4)$$

Here, $V_{id}(A)$ is the magnitude of the oxidation state, which equals the BVS of ion A at the ideal equilibrium site, and CN_{min} is a minimum coordination number for A (in this work, CN_{min} = 4). For structures where more than one type of cation is involved, cation−cation repulsion by unlike cations also has to be accounted for by an additional penalty function when analyzing the cation pathways.

3. Results and Discussion

3.1. Non-Ambient XRD and Structure Refinement. Results of the Rietveld refinements for the structure of $Sc_2(WO_4)_3$ are summarized in Table 1. As an example, Figure 1 shows the refinement of 300 K data (measured in the heating chamber). Cell parameters of heating and cooling cycle agree. Using the heating cycle data listed in Table 1 as a calibration curve, temperatures of the cooling cycle data can be determined from the lattice constants with an accuracy of ±20 K. From the temperature variation of the lattice constants plotted in Figure 2, it can be seen that there is a minute offset between our results obtained in high- and low-temperature diffraction setups, but the trend is identical. The thermal expansion coefficients derived from these measurements are given in Table 2. For the lower-temperature range, the values are in reasonable agreement to those found by Evans et al.,[13] whereas earlier single crystal dilatometric data by Balashov et al.[32] are not consistent with our findings. For the high-temperature range, where no diffractometric refer-

(24) Kharton, V. V.; Marques, F. M. B. *Solid State Ionics* **2001**, *140*, 381–394.
(25) Cerius2, version 4.9; Accelrys Inc.: San Diego, 2003.
(26) Materials Studio, version 4.2; Accelrys Inc.: San Diego, 2007.
(27) Rappé, A. K.; Casewit, C. J.; Colwell, K. S.; Goddard, W. A.; Skiff, W. M. *J. Am. Chem. Soc.* **1992**, *114*, 10024–10035.
(28) Verlet, L. *Phys. Rev.* **1967**, *159*, 98–103.
(29) Brown, I. D., *The Chemical Bond in Inorganic Chemistry−The Bond Valence Model*; Oxford University Press: New York, 2002.
(30) Adams, S. *Acta Crystallogr., Sect. B* **2001**, *57*, 278–287.
(31) Adams, S. softBV; http://www.softBV.net.
(32) Balashov, V. A.; Vorona, G. I.; Maier, A. A.; Proshina, O. P. *Izv. Akad. Nauk SSSR, Neorg. Mater.* **1975**, *11*, 1713.

Table 1. Cell Dimensions as a Function of Temperature

T (K)	a (Å)	b (Å)	c (Å)	V (Å^3)	R_{wp} (%)[b]	$R(F^2)$ (%)
11[a]	9.68300(11)	13.31784(15)	9.59151(11)	1236.889(31)	6.76	4.12
50[a]	9.68301(11)	13.31962(15)	9.59143(11)	1237.045(30)	7.51	4.24
100[a]	9.68232(12)	13.32028(17)	9.59088(12)	1236.947(33)	6.87	3.84
150[a]	9.68078(7)	13.32122(10)	9.58941(7)	1236.650(20)	7.24	3.94
200[a]	9.67845(8)	13.32378(11)	9.58721(8)	1236.305(22)	7.86	4.46
250[a]	9.67514(7)	13.32701(9)	9.58449(7)	1235.830(18)	7.43	4.12
300[c]	9.67132(9)	13.33083(13)	9.58179(9)	1235.341(25)	6.95	3.88
300[d]	9.67144(7)	13.32617(9)	9.58110(7)	1234.842(17)	5.96	4.16
350	9.66691(6)	13.33105(8)	9.57804(6)	1234.314(16)	5.94	4.49
400	9.66276(6)	13.33496(8)	9.57504(6)	1233.769(15)	5.91	4.52
450	9.65894(6)	13.33824(8)	9.57242(6)	1233.247(15)	6.04	4.70
500	9.65542(5)	13.34124(7)	9.57000(5)	1232.762(14)	5.88	4.90
550	9.65206(5)	13.34383(7)	9.56777(5)	1232.273(13)	5.78	5.10
600	9.64871(5)	13.34598(7)	9.56563(5)	1231.781(13)	5.87	5.44
650	9.64531(5)	13.34780(7)	9.56346(5)	1231.235(13)	6.04	5.71
700	9.64246(5)	13.34917(7)	9.56139(5)	1230.718(13)	5.92	6.01
750	9.63955(5)	13.35026(7)	9.55959(5)	1230.241(13)	6.00	6.20
800	9.63696(5)	13.35110(7)	9.55783(5)	1229.748(13)	6.03	6.33
850	9.63440(5)	13.35201(7)	9.55607(5)	1229.280(13)	6.16	6.63
900	9.63194(5)	13.35293(7)	9.55447(5)	1228.844(13)	6.13	6.85
950	9.62970(5)	13.35375(7)	9.55309(5)	1228.457(13)	6.16	6.83
1000	9.62760(5)	13.35461(7)	9.55164(5)	1228.081(13)	6.25	6.96
1050	9.62547(5)	13.35535(8)	9.55038(5)	1227.725(14)	6.21	7.15
1100	9.62355(6)	13.35626(8)	9.54910(6)	1227.390(14)	6.22	7.38
1150	9.62166(6)	13.35709(8)	9.54792(6)	1227.073(14)	6.04	7.28
1200	9.61988(6)	13.35768(8)	9.54671(6)	1226.746(15)	5.96	7.65
1250	9.61797(6)	13.35797(8)	9.54552(6)	1226.376(15)	5.93	7.91
1300	9.61588(6)	13.35786(9)	9.54392(6)	1225.894(17)	6.06	8.02

[a] Refined from 3 sets of XRD diffraction data. [b] Weighted profile R-factor after background subtraction. [c] Measured in a cryostat. [d] Measured in a high-temperature chamber.

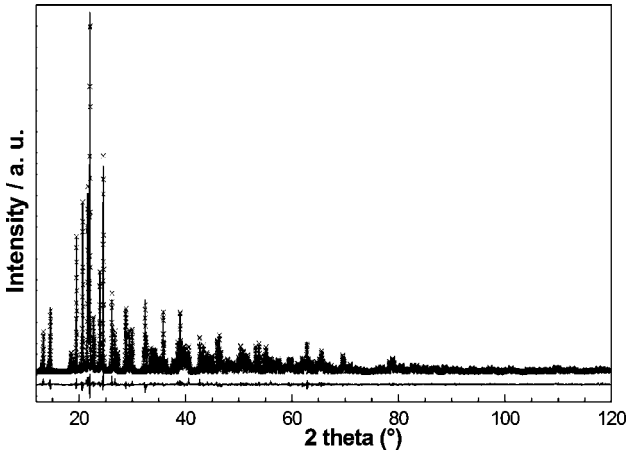

Figure 1. Refinement of $Sc_2(WO_4)_3$ structure at 300 K with final R_{wp} = 7.74%. Observed (×), calculated (line), and observed − calculated (lower line).

ence data exist, we find a reduction in the magnitude of all linear expansion coefficients.

Beyond the variation in the unit cell, the variation in the freely Rietveld refined atomic coordinates provides further insight into the local mobility of the building blocks of the $Sc_2(WO_4)_3$ structure. For such an open framework structure that permits large angle rotations of nearly rigid building blocks, the apparent distance between the average positions of two bonded atoms that is observed in an XRD structure determination does not match the "true" average instantaneous distance. (For a more detailed discussion see for example ref 13). In brief, a negative thermal expansion can be expected if such correlated rotations dominate over uncorrelated vibrations of the individual atoms, which via the anharmonicity of the interaction potential are the source

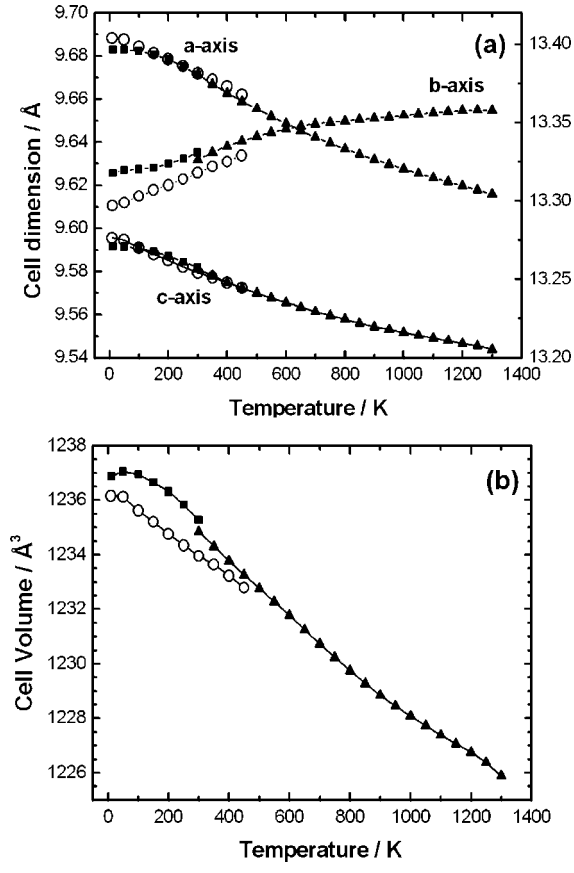

Figure 2. Temperature dependence of (a) unit-cell parameters and (b) cell volume of $Sc_2(WO_4)_3$ as determined from high-temperature (▲) or low-temperature (■) XRD data in this work. Neutron diffraction data by Evans[13] (♀) are shown for comparison.

of the normal thermal expansion. A high correlation of the rotations can be expected if the interatomic interactions are

Table 2. Thermal Expansion Coefficients

	this work[a,c] ($\times 10^{-6}$ K^{-1})		Evans[a]	Balashov[b]
	100−700 K	700−1300 K	($\times 10^{-6}$ K^{-1}) 50−450 K	($\times 10^{-6}$ K^{-1}) 293−873 K
a	−7.37	−4.3	−6.49	−5.45
b	3.97	1.09	5.61	4.43
c	−5.41	−2.82	−5.73	−1.6
V	−8.8	−6.02	−6.44	n.a.

[a] From powder diffraction. [b] From single-crystal dilatometry. [c] Two linear regions are observed in this work: one is 100−700 K, the other is 700−1300 K, whereas data for T < 100K deviate therefrom.

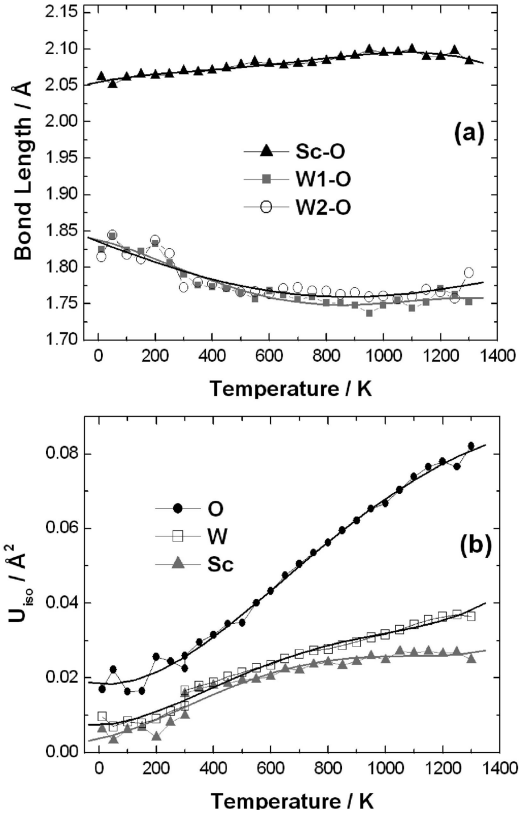

Figure 3. Temperature dependence of (a) the average apparent bond length and (b) of the atomic displacement parameters in $Sc_2(WO_4)_3$ as determined from Rietveld refinements.

both strong and directional. In Figure 3a this apparent average bond length is plotted as a function of temperature. When T increases, the Sc−O bond length increases, whereas W−O bonds appear to become shorter. This apparent displacement of the O toward the W is a consequence of the increase in the amplitude of the O atom vibration perpendicular to the bond axis. The finding that this results in an apparent shortening of the bond only for W−O bonds, but not for Sc−O bonds, suggests that the motion of the O is more effectively controlled by the nearby W. To a good approximation, the polyatomic anion WO_4^{2-} may be regarded as a rigid unit (while the ScO_6 coordination polyhedron is significantly less rigid). Therefore, we expect that the energy to break the more ionic Sc−O interaction should be significantly lower than the energy to break the more covalent W−O bond.

For the sake of refinement stability we have limited the direct evaluation of thermal displacement from the Rietveld refinement to one isotropic atomic displacement parameter per atom type. Still the analysis of the refined values of U_{iso} displayed in Figure 3b gives some indications on the differences between the local mobilities of the various potential charge carriers. As expected, the highest U_{iso} at each temperature is observed for the oxygen atoms, both because oxygen is the lightest atom and because the apparent U_{iso} includes contributions from the rotation of the rigid polyatomic unit that might cause the saturation tendency at elevated temperatures. It should be noted that in the high temperature range the value of U_{iso} for W^{6+} is larger than the one of the (significantly lighter) Sc^{3+} ion, which points toward an unusually high local mobility of the W atom, including but not necessary limited to the rotation of the WO_4 units.

3.2. Computational and Experimental Studies of the Dynamic Structure. *3.2.1. Modification of Forcefield to Reproduce Volume and NTE.* In this work, MD simulations are employed both directly to analyze diffusion coefficients and thereby the ionic conductivities of mobile charge carriers and as a basis for a dynamic ion transport pathway analysis. To ensure that the forcefield parameters are realistic, we first tried to reproduce not only the lattice constants, but also the characteristic negative thermal expansion behavior by NPT simulations.

The structure of $Sc_2(WO_4)_3$, as shown in Figure 4, is usually regarded as being a three-dimensional framework built up by WO_4 tetrahedra that are corner-linked to ScO_6 octahedra. As sketched in Figure 5, the observed reduction of the apparent W−O distances is due to large amplitude librations of the building blocks that directly translate into a reduced Sc−W distance and thus into a negative thermal expansion in the W−Sc direction (cf. Evans[13]). The standard universal forcefield (UFF)[27] as implemented in Cerius[2] in combination with QEq[33] charges clearly fails to reproduce the experimental volume or the negative thermal expansion behavior (room temperature unit cell volume V_{RT}: 1234.8 Å^3 (experimental), 1951.3 Å^3 (UFF) volume expansion coefficients for 100K < T < 700K: $\alpha = -8.8 \times 10^{-6}$ K^{-1} (experimental), $+14.1 \times 10^{-6}$ K^{-1} (UFF)). To this end, we revised the Sc−O interaction in the UFF, replacing original Lennard Jones-type nonbonded interactions by the more realistic, yet computationally more expensive Morse potential (see eq 5).

$$V(r) = D_0((1 - e^{-\frac{y}{2}(\frac{r}{r_0}-1)})^2 - 1), \text{ where } y = 2r_0\sqrt{k/2D_0} \quad (5)$$

with the parameters bond energy D_0, equilibrium bond distance r_0, and potential width exponent y, which depends on r_0, D_0, and the bond force constant k, while the calculation of fractional charges for the Coulomb interactions by means of the QEq formalism remained unchanged. The chosen form of the interaction potential $V(r)$ has to allow that Sc−O bonds can be broken with a finite activation energy, because any of the considered ion transport mechanisms would require the breaking of a Sc^{3+}−O bond. Thereby, even if the accuracy of the chosen parameters is difficult to prove, it should only have a minor influence on which ion is the most mobile species. In this work, we use the parameters

(33) Rappé, A. K.; Goddard, W. A. *J. Phys. Chem.* **1991**, *95*, 3358–3363.

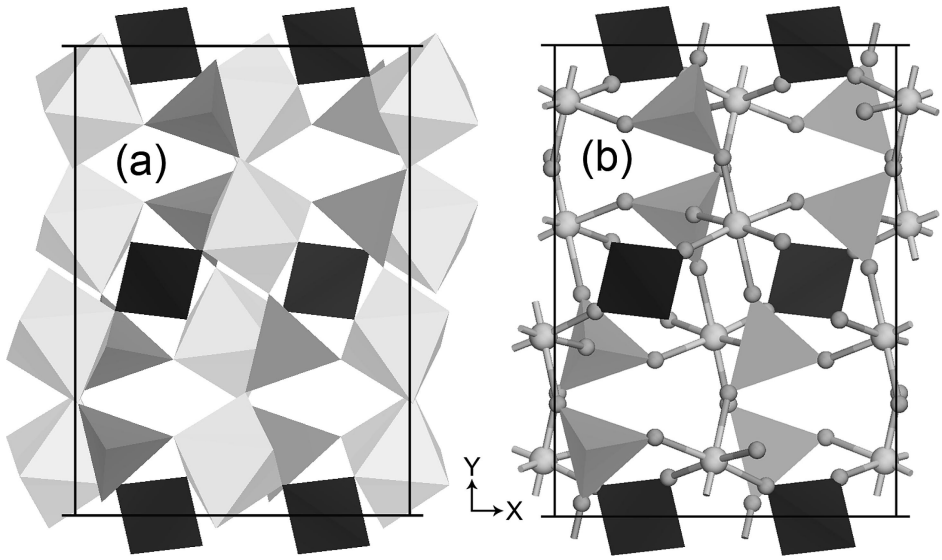

Figure 4. Projection of the $Sc_2(WO_4)_3$ structure on the $a-b$ plane showing (a) ScO_6 as light octahedra; $W(1)O_4$ as dark and $W(2)O_4$ as light tetrahedra (O not shown) (b) Sc as large, O as small spheres, and WO_4 tetrahedra as in graph (a). From the observations reported in this work, it appears to be more appropriate to use version (b) emphasizing the WO_4^{2-} groups as structural units.

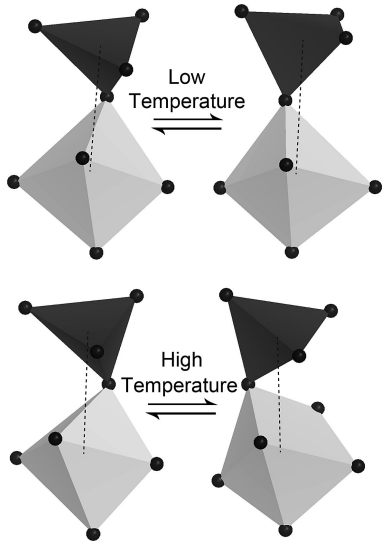

Figure 5. Schematic representation of how the negative thermal expansion can be linked to the increase in amplitude of a rocking mode of nearly rigid building blocks. Top: dark WO_4 tetrahedron, bottom light gray ScO_6 octahedron; O shown as spheres. The average W−Sc distance (dotted line) drops from 3.776 Å at 50 K to 3.758 Å at 1000 K.

D_0(Sc−O) = 2 kcal/mol, r_0 (Sc−O) = 2.4 Å and $y = 11$ as simulations using these values come closest to a reproduction of the unit-cell volume and thermal expansion behavior. With these parameters and QEq charges the breaking of a Sc−O bond requires a dissociation energy of 90.6 kcal/mol, and for equilibrium distances the bond energy is dominated by the Coulomb interaction. For W−O bonds we assumed a simple harmonic bond stretching term (spring constant k_0 = 600 kcal/(mol Å^2), r_0 = 1.75 Å), so that the simulation cannot yield any predictions on mechanisms involving the breaking of W−O bonds. For 300 K the simulation yields a cell volume of 1233.1 Å^3 closely matching the experimental unit cell volume of 1234.8 Å^3. The negative thermal expansion along the a and c direction (and positive expansion along the b direction) is reproduced in our MD simulations over a limited temperature range, though the expansion coefficient $\alpha = -2.0 \times 10^{-6}$ K^{-1} averaged over the temperature range

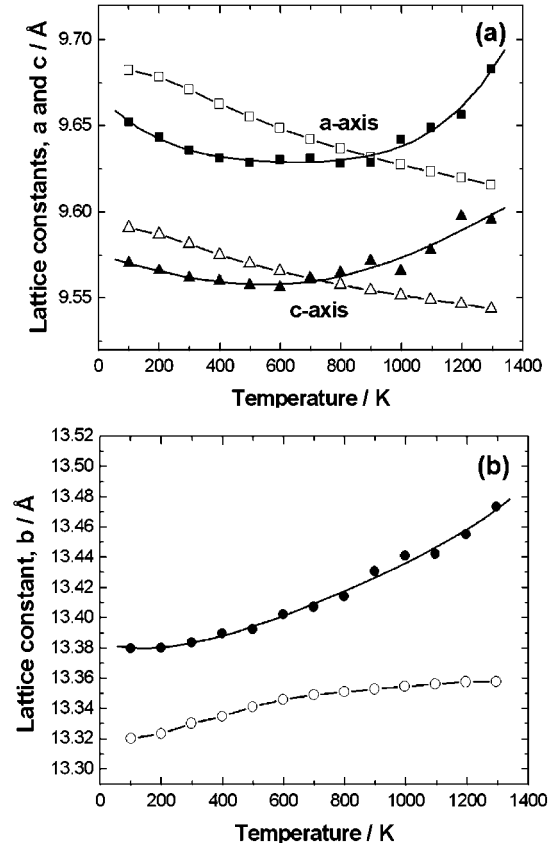

Figure 6. Variation of lattice constants a (squares), c (triangles), and b (circles) of $Sc_2(WO_4)_3$ as a function of temperature in a NPT simulation (solid), which are compared with experimental data (hollow) from this work.

100 K < T < 700 K is still underestimated by the revised forcefield. The variation of the simulated lattice constants is plotted in Figure 6.

A further common way to adjust forcefields by fitting also the compressibility is difficult to realize in this case due to inconsistent experimental literature data on the pressure where an orthorhombic to monoclinic phase transition occurs

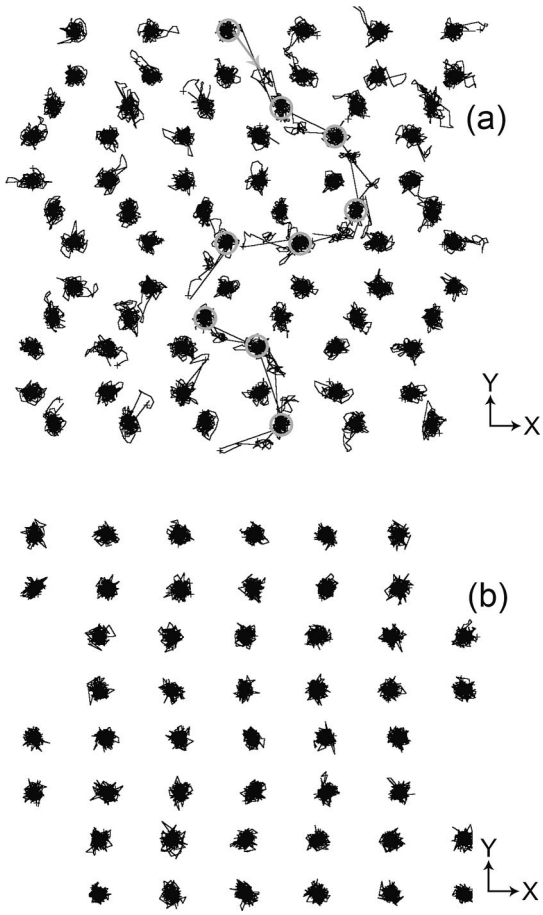

Figure 7. Trace of the motion of (a) W atoms (initial positions of the nine moving WO_4^{2-} groups indicated as circles; the first hop from an equilibrium site to an interstitial tungstate site is marked by an arrow); and (b) Sc atoms for the NVT simulation of $Sc_2(WO_4)_3$ at $T = 1300$ K.

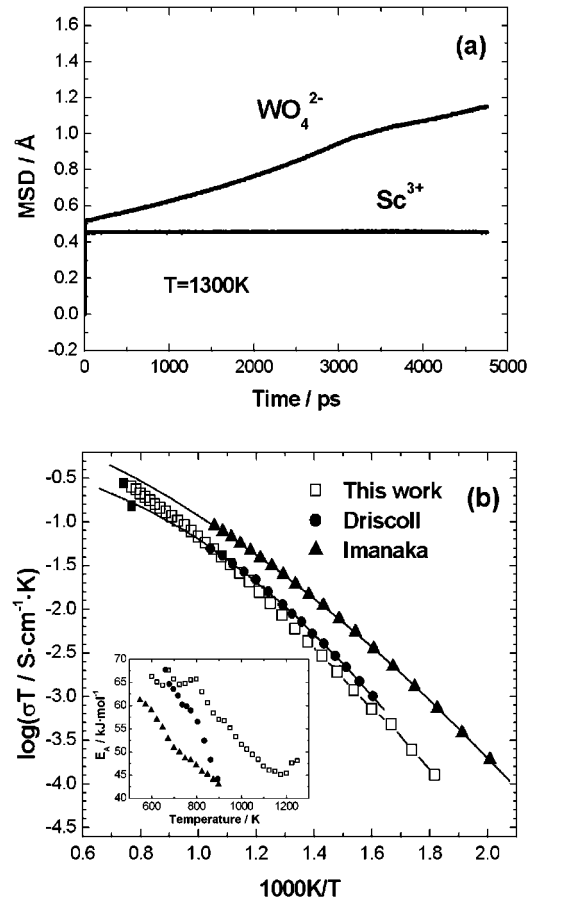

Figure 8. (a) Simulated mean square displacement of WO_4^{2-} and Sc^{3+} vs time for a NVT simulation of $Sc_2(WO_4)_3$ at $T = 1300$ K. (b) Comparison of simulated conductivity (■), experimental conductivities obtained in this work (□); experimental data by Driscoll et al.[11] (●), and by Imanaka et al.[2] (▲) are shown for comparison. The inset graph shows the variation of the activation energy with temperature as derived from the three sets of experimental conductivity data (using the same symbols).

(0.3 GPa according to Varga et al.,[34] 0.6 ± 0.4 GPa according to N.Grag et al.[35]). For the small pressure range below the transition pressure, the anisotropy of the compressibility obtained in simulations with our forcefield qualitatively agree with data by Varga. Detailed results of the ongoing pressure-dependent studies will be published elsewhere.

3.2.2. Conductivity. With this modified forcefield, NVT simulations were performed for 4 temperatures in the range 1200−1350 K for the equilibrated lattice constants at each temperature. The simulated periods ranged from 8.5 ns for $T = 1350$ K to 13.5 ns for $T = 1200$ K. For the simulations at $T = 1300$ and 1350 K, hops of WO_4^{2-} groups are observed, whereas none of the simulations indicated local hops of Sc^{3+} ions. (As mentioned above, we cannot expect O^{2-} hops because of the choice of the forcefield). A more detailed analysis of the MD simulation trajectory reveals that several hops are highly correlated. This can be visualized by plotting the trace of the moving WO_4^{2-} group. Figure 7a, produced with gOpenMol,[36] shows traces for the motion of W atoms (the centers of the WO_4^{2-} group). As seen in Figure 7a, nine WO_4^{2-} groups formed a pathway through the supercell. Thereafter the initial defect vanishes again when the ninth WO_4^{2-} fills the translation copy of the vacancy created in the initial step. The traces for Sc atoms are also shown in Figure 7b, illustrating that the simulated Sc atoms just oscillate around their equilibrium positions and do not exhibit any tendency to leave these sites. Thus according to the MD simulations obviously WO_4^{2-} and not Sc^{3+} is the diffusing charge carrier in $Sc_2(WO_4)_3$.

As mentioned above, WO_4^{2-} hops are observed for the higher simulated temperatures 1300 and 1350 K only. From these hops, the time dependence of the mean squared displacement (MSD, see Figure 8a) for WO_4^{2-} and (therefore via the Nernst−Einstein equation) the conductivity is roughly assessed. Simulated and experimental conductivity data are plotted in Figure 8b. along with experimental data from the literature.[2,11] Data by Driscoll for the limited temperature range 625−960 K are consistent with our findings, whereas values reported by Imanaka are somewhat larger. Differences might be partially related to differences in the density of the samples. When comparing experimental and simulated conductivities, it should be noted that, as discussed further below, the obtained absolute conductivity values will substantially depend on defect creation steps that occur only rarely even for the rather long simulated periods as well as

(34) Varga, T.; Wilkinson, A. P.; Jorgensen, J. D.; Short, S. *Solid State Sci.* **2006**, *8*, 289–295.
(35) Garg, N.; Murli, C.; Tyagi, A. K.; Sharma, S. M. *Phys. Rev. B* **2005**, *72*, 7.
(36) Laaksonen, L. *J. Mol. Graph.* **1992**, *10*, 33–34.

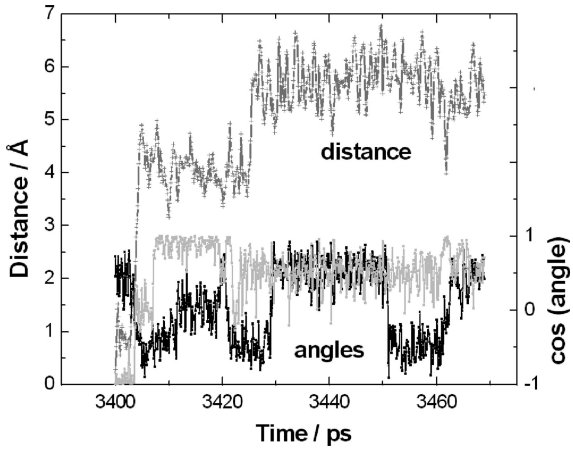

Figure 9. Correlation between the variation of the distance of a WO_4^{2-} (with respect to its position at $t_0 = 3400$ ps) and the change in the orientation angle of two W−O bonds (with respect to the *x* axis) over 69 ps with a resolution of 0.1 ps.

on the length of the chain of migration steps before the defect vanishes (which may be affected by the size of the chosen supercell). Thereby the observed good agreement with both our own and literature data on the experimental conductivity should be taken with care.

The inset in Figure 8b emphasizes the variation of the experimental activation energy. We find a plateau of the activation energy of 65 kJ/mol for $T < 800$ K, and then a gradual decrease to a value of ca. 45 kJ/mol for 1100−1200 K and a slight increase for the highest temperature range (1200−1300 K). Although the range of observed activation energies is similar for the literature data, the temperature where the decrease in activation energy sets in varies significantly.

3.2.3. Analysis of WO_4^{2-} Rotation and Transport Mechanism. As the hopping of the relatively large WO_4^{2-} in the solid state has so far not been observed, we tried to analyze the mechanism of the polyatomic anions in this novel type of solid electrolytes more in detail. We noted that the hopping of WO_4^{2-} group is inevitably accompanied by a rotation of the tetrahedron. In Figure 9 the diffusion of the WO_4^{2-} group is tracked by the variation of the distance of the central W from its position in the reference frame. The time steps of elementary diffusion steps are then compared to time steps where rotations of the WO_4^{2-} group occur. The tetrahedron rotations are registered as changes in the orientation of W−O bonds, which is simply expressed by the angle between the bonds and the *x* axis. Orientation angles are traced for two different W−O bonds to capture all rotations. It is found that all elementary hopping steps, such as the ones observed at $t = 3404$ and 3426 ps, are accompanied by reorientations, so that one might rather describe the elementary transport step as a rolling of the WO_4^{2-} group to its new position. On the other hand, some further rotations shown in Figure 9, such as the one at $t = 3450$ ps, are not connected to translational diffusion steps. On the basis of the selected range of frames in Figure 9, it is also noted that the values and fluctuations of the W−O bond length (1.698 ± 0.072 Å) or O−W−O bond angles (106 ± 10°) around the time steps of the hopping processes exceed the normal fluctuations (1.699 ± 0.067 Å, 109 ± 7°) only slightly, supporting the model of WO_4^{2-} being a rather rigid building block.

It may be noted that the finding of anion rotation in solid electrolytes as such is not new. The motion of monovalent cations under the influence of rotation of anions such as SO_4^{2-} and PO_4^{3-} has been the subject of long-standing discussions (see, for example, refs 37−39), but the proposed transport mechanism for $Sc_2(WO_4)_3$ obviously differs from such rotator phases in that the tungstate anion in $Sc_2(WO_4)_3$ is the mobile species, rather than the facilitator for a cation motion.

3.2.4. Bond Valence Analysis of Long-Range Transport in $Sc_2(WO_4)_3$. Bond valence analyses for the geometry optimized structure of $Sc_2(WO_4)_3$ have been performed in our previous work and will be only briefly summarized here.[16] Bond valence maps of Sc^{3+} and O^{2-} show that only isolated regions of low bond valence mismatch value exist for these two ions. In the case of O^{2-}, these regions again indicate that the lowest-energy local motion should correspond to the collective rotation of the entire tungstate ion. When we however analyze the BVS mismatch for WO_4^{2-} (treating it as a pseudoatom), extended regions of low bond valence sum mismatch are observed that link occupied and unoccupied tungstate sites thereby forming pathways for a long-range diffusion of WO_4^{2-}. Still, it should be kept in mind that these preliminary calculations are based on static average structure models and that treating tungstate as a pseudoatom may not capture essential details of critical configurations, especially for the motion of a polyatomic deformable species that as we have seen undergoes reorientations during the hopping.

Thus, a more detailed dynamic bond valence analysis was performed in this project by calculating bond valence models of the instantaneous ion transport pathways for series of time frames from the MD simulation trajectory. For each time step, the respective pathway model was constructed from the instantaneous atomic positions of the MD trajectory. Figure 10 monitors the evolution of BV ion transport pathways for a series of time steps from such a dynamic ion transport pathway model. As shown in Figure 10, characteristic features of the ion transport pathways remain stable over periods exceeding the time scale of local hopping processes, though there is substantial fluctuation of the regions accessible at every instant. As had been found previously for other ion conductors,[40] ion transport pathways remain limited to a small portion of the total volume. Once a defect has been formed, ion transport clearly follows this fluctuating network of instantaneous pathways, underlining the predictive power of the bond valence method. There is however consistently an exception at the beginning of the chain of correlated local hopping processes. Even in the fully stoichiometric ensemble local hops of tungstate groups to nearby interstitial sites are possible, but from these interstitial

(37) Andersen, N. H.; Bandaranayake, P.; Careem, M. A.; Dissanayake, M.; Wijayasekera, C. N.; Kaber, R.; Lunden, A.; Mellander, B. E.; Nilsson, L.; Thomas, J. O. *Solid State Ionics* **1992**, *57*, 203–209.
(38) Jansen, M. *Angew. Chem., Int. Ed.* **1991**, *30*, 1547–1558.
(39) Lunden, A. *Solid State Commun.* **1988**, *65*, 1237–1240.
(40) Müller, C.; Zienicke, E.; Adams, S.; Habasaki, J.; Maass, P. *Phys. Rev. B* **2007**, *75*, 014203.

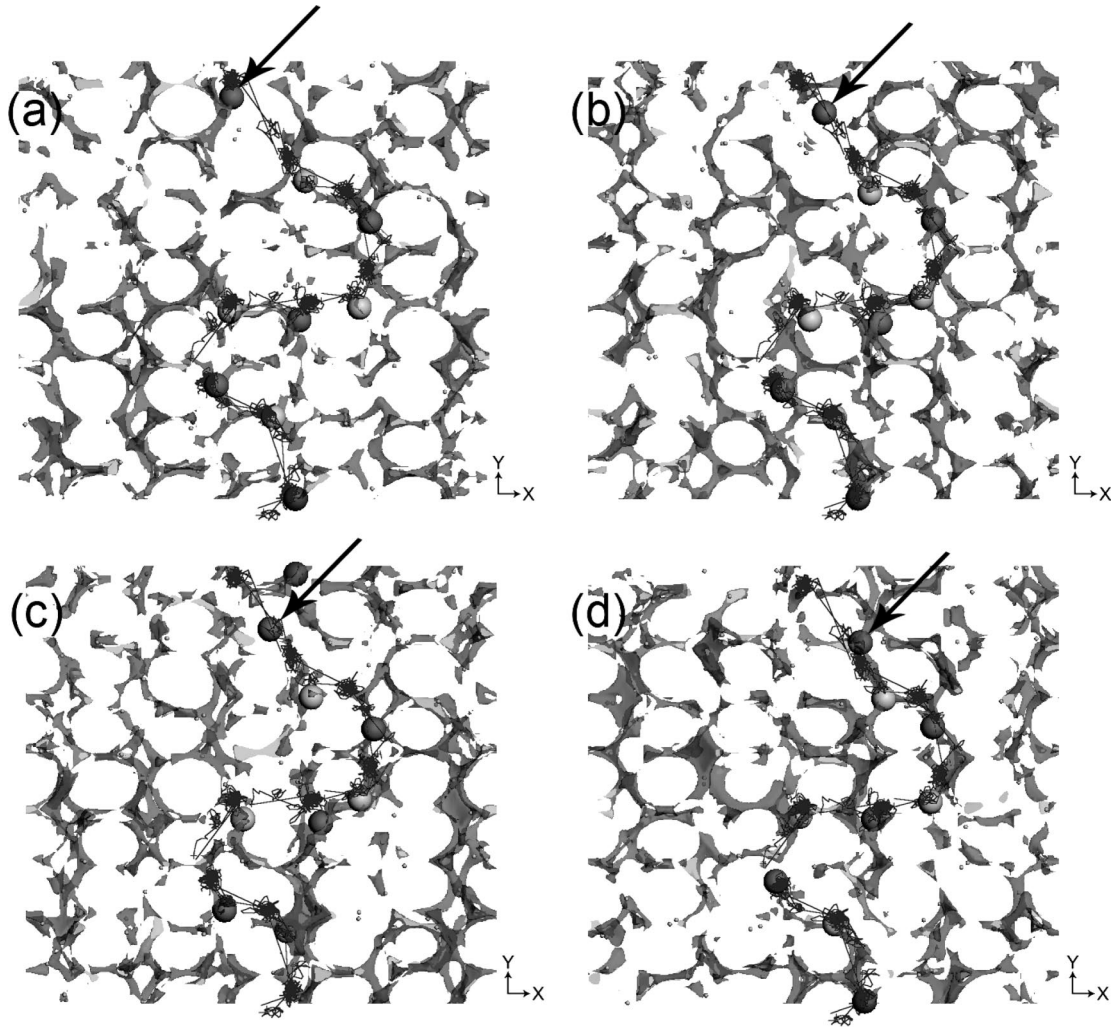

Figure 10. Four selected frames from a dynamic bond valence analysis with nine moving WO_4^{2-} groups (marked by gray spheres) forming a pathway through the supercell (total time interval between frames (a) t= 3403.3 ps and (d) t = 3404.5 ps is 1.2 ps). The gray isosurface represents a BVS model of the instantaneous WO_4^{2-} pathways (i.e., regions of BVS mismatch $|\Delta V| < 0.25$ valence units for WO_4^{2-}). Traces of the W atoms that hop within a 69 ps period of the MD simulation (same period as for Figure 9) are superimposed on this BVS pathway landscape.

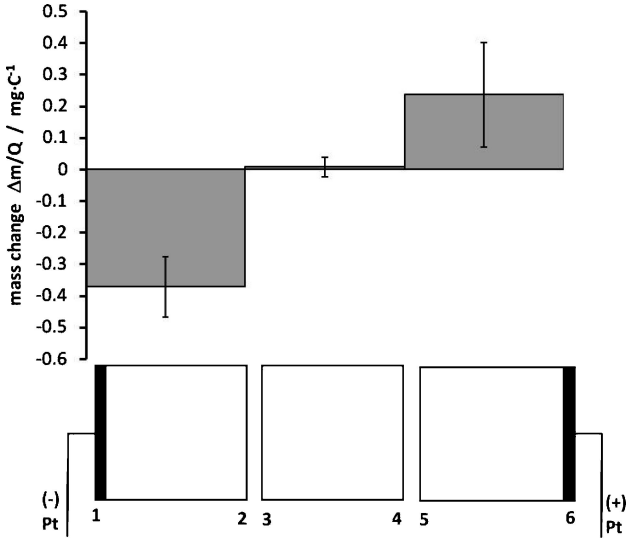

Figure 11. Schematic setup of Tubandt-type cell experiments with stacks of 3 $Sc_2(WO_4)_3$ disks for T = 940 °C. Average mass changes and their standard deviations are indicated for the individual disks as observed in the four experiments listed in Table 3.

Table 3. Mass Changes for 4 Tubandt Experiments

exp.	$\Delta m(-)$ (mg)	$\Delta m(+)$ (mg)	Q (C)[a]	$\Delta m(-)/Q$ (mg/C)	$\Delta m(+)/Q$ (mg/C)
I	−6.1	6.0	15	−0.41	0.40
II	−32.2	21.1	88	−0.37	0.24
III	−3.4	0.3	18	−0.19	0.02
IV	−3.4	1.1	10	−0.34	0.11

[a] Q, passed charge in Coulombs; initial thickness of individual disks 1.4 ± 0.1 mm in all listed experiments.

sites (discernible in Figure 7a as sites with short residence times next to the zigzag line of equilibrium sites), the most probable subsequent step is the hopping back to the equilibrium site.

The interstitial sites observed in the simulations are in the close vicinity of 3 types of nodes of the BV mismatch pathways: (A: x = 0.35, y = 0.38, z = 0.7/8; B: x = 0.35, y = 0.38, z = 5/8; C: x = 0.23, y = 0.27, z = 1/2), while no moving ions were found for a further node of the pathway (D: x = 1/4, y = 1/2, z = 0.55). Each tungsten atom W1 is surrounded by two interstitials type A, each W2 by three interstitial sites (1 B + 1 C + 1 D). Pathways also link interstitial sites A and B sites as well as A and C, leading to a three-dimensional network of pathways. Pathways connecting W1 with W2 sites or two W2 sites with each other involve at least two intermediate interstitial sites (W1−A−B−W2,

W1−A−C-W2, W2−B−C−W2), whereas a transport from one W1 site to another W1 site would have to involve 4 interstitial sites (W1−A−B−C−A−W1). Distances between neighboring sites within this pathway network are in the range 1.9−2.6 Å.

In the cases studied more in detail, long-range transport was initiated only when a tungstate ion with a high activation energy (i.e., capable of leaving the low BV mismatch region) approached another tungstate ion that just left its equilibrium site to one of the nearby low-energy interstitial sites and pushes it away along the BV pathway toward the next equilibrium site. This interstitialcy-like transport mechanism is then repeated several times within a short period until the last interstitial ion again finds a vacancy (in the simulations there was always just one vacancy present and the chain of transport steps either formed a loop or led to the vacancy in a translation copy of the original simulation cell). Thus a typical transport event would involve one step that does not follow the bond valence pathway, such as the one marked by arrows in Figure 10 starting a series of correlated ion hops along the bond valence pathway.

It should be reemphasized that the tungstate Frenkel defect creation is obviously a rare high energy process. The actually observed activation energy will depend on the ratio between the high energy defect creation and the chain of lower energy tungstate rearrangements made possible by the defect creation. With the limited size of the model (1224 atoms, which was enforced by the need to run the simulations over several nanoseconds) it is difficult to judge, whether the observed density of vacancies and thereby the number of low-energy charge transport steps between defect creation and annihilation is realistic. Thus it cannot be ruled out that the reasonably good agreement between the simulated and experimental conductivities might be to some extent a coincidence. The higher activation energy observed in the simulations might be a sign that the typical chain length is longer than the 7−9 steps observed in our simulations. Ongoing MD simulations with artificially created vacancies in the supercell may help to clarify whether the variation of the experimentally observed conductivity values for samples from different groups may be due to a different defect concentration in these materials.

3.3. Mass and Charge Transfer Experiments in Tubandt-Type Cells with $Sc_2(WO_4)_3$. Our EMF experiments at 940−990 °C with active loads (Gorelov's method) confirm that $Sc_2(WO_4)_3$ is a purely ionic conductor with an ionic transference number ~1.00, while earlier literature reported $t > 0.92$ (based on measurements without active loads).[1] In the literature, the results of electrolysis experiments using a single solid electrolyte disk in a (Pt)|$A_2(WO_4)_3$|(Pt) cells have been used as evidence of trivalent-cation conduction. However, the chemical and phase composition of cathode and anode regions after electrolysis would be identical, independent of whether Sc^{3+} or WO_4^{2-} are the main ionic carriers. For $Sc_2(WO_4)_3$, one expects the formation of Sc_6WO_{12} at the $Sc_2(WO_4)_3|Pt^{(-)}$ boundary and WO_3 at the $Sc_2(WO_4)_3|Pt^{(+)}$ boundary, regardless of the carrier.

The setup for the Tubandt-type experiment, shown in Figure 11 consists of three $Sc_2(WO_4)_3$ ceramic disks between two platinum electrodes:

$$(-)|(-)Sc_2(WO_4)_3|Sc_2(WO_4)_3|(+)Sc_2(WO_4)_3|Pt(+) \quad (6)$$

If Sc^{3+} ions are mobile, they will migrate from the positively charged side toward the negatively charged side according to

$$(+)Sc_2(WO_4)_3 \rightarrow 16Sc^{3+} + 24WO_3 + 12O_2 + 48e- \quad (7)$$

$$(-)Sc_2(WO_4)_3 + 16Sc^{3+} + 12O_2 + 48e^- \rightarrow 3Sc_2WO_{12} \quad (8)$$

This should decrease the mass of the $(+)Sc_2(WO_4)_3$ disk and increase the mass of the $(-)Sc_2(WO_4)_3$ disk. On the other hand, if the WO_4^{2-} ion is the main ionic carrier, it will migrate from the negatively charged side toward the positively charged side, according to

$$(-)3Sc_2(WO_4)_3 + 16e^- + 4O_2 \rightarrow Sc_6WO_{12} + 8WO_4^{2-} \quad (9)$$

$$(+)8WO_4^{2-} \rightarrow 8WO_3 + 4O_2 + 16e^- \quad (10)$$

which should result in a decrease in the mass of the $(-)Sc_2(WO_4)_3$ disk and an increase in the mass of the $(+)Sc_2(WO_4)_3$ disk with the deposition of WO_3.

Experiments with cells of type (6) were performed at different potential−current conditions and temperatures. The resulting mass changes for 4 typical experiments at $T = 940$ °C are summarized in Table 3. The Q-weighted average mass transfer for these cells is sketched in Figure 11. In all experiments, we consistently observed a decrease in the mass of the negatively charged section of $Sc_2(WO_4)_3$, which indicates that the mobile species is negatively charged. However, the quantity of the products formed on the electrodes or in near-electrodes regions was too low for conclusive determination by XRD or microprobe (10−88 Coulombs ≈ $1-9 \times 10^{-4}$ F), but suggest that Sc_6WO_{12} is formed for boundary (1) in Figure 11 and WO_3 at boundary (6), which also changed its color to WO_3-like. The spotty nature of the color changes also highlights that for most of the experiments the effective contact area between the ceramic disks included only a small fraction of the geometric disk surface. Thus, the data obtained may serve as the first qualitative experimental evidence of WO_4^{2-} transport in solid $Sc_2(WO_4)_3$. Despite the small amount of charges passed, the decrease of negative mass change of the $(-)Sc_2(WO_4)_3$ section was matched in most experiments by an increase of $(+)$ $Sc_2(WO_4)_3$-disk though with a Coulomb efficiency of only 30% when assuming a transport according to eqs 9 and 10 (or an impossible Coulomb efficiency of 200% if the mechanism follows eqs 7 and 8). Obviously the high voltage required to achieve a measurable mass transfer also gives rise to parallel charge transfer reactions that do not involve a mass transfer. For higher temperatures and longer electrolysis periods, the interpretation becomes more complex because of the rising influence of WO_3 volatility during the electrolysis, which contributes to a more pronounced imbal-

ance between the mass decrease and increase of opposite disks. These findings harmonize with our recent detailed Tubandt-type experiments for the isostructural $In_2(WO_4)_3$.[10]

4. Concluding Remarks

Through the combination of X-ray data, impedance spectroscopy, Tubandt-type DC electrolysis, molecular dynamics simulations and their bond valence analysis, characteristics of the unusual charge transport in $Sc_2(WO_4)_3$-type solid electrolytes can be revealed. From a synopsis of our results it has to be concluded that WO_4^{2-}, the rigid unit with the lowest charge in the system is the mobile species and that the elementary transport steps combine features of an intersticialcy mechanism with a unique rotation component. Typically, a rotation step leads to an "activated transition state" that can stabilize by slight further reorientations of the WO_4^{2-} and its environment (so that no transport occurs) or allow for a transport step and a further rotation step as a part of the relaxation at the target site. The proposed "rock and roll" WO_4^{2-} ion transport mechanism not only rationalizes the ionic conductivity. It is also consistent with a variety of further hitherto controversially discussed experimental results. The suggested ion transport may be regarded as an O^{2-} vehicle mechanism, but it does not involve oxide ion vacancies; therefore no dependence of polarizability on the O_2 partial pressure is to be expected in polarization experiments. The reported conductivity increase with increasing size of the trivalent cation can be rationalized as an increase of free volume for the mobile tungstate ion. Our Tubandt-type measurements confirm that the effective charge carrier is an anion. The rise in the activation energy with decreasing temperature may be traced back to the more effective blocking of rotations of tetrahedra that are necessary to allow the migration step. Although $Sc_2(WO_4)_3$ should no longer be regarded as the prototype of a trivalent cation conductor, it turns out that the pioneering work by Imanaka and coworkers has led to the prototype of a promising new class of polyanion conductors.

Acknowledgment. This Materials World Network project was cofunded by A-Star SERC (NSF-MWN 062 119 0009), NSF (DMR-060288), and RFBR (06-03-90170-NSF).

Supporting Information Available: Results of the structure refinement at various temperatures listed in Table 1 in CIF format. Detail from the MD simulation trajectory and superimposed instantaneous bond valence pathway model as an avi animation. This material is available free of charge via the Internet at http://pubs.acs.org.

CM800466Y